

Rapid room-temperature synthesis of nanocrystalline spinels as oxygen reduction and evolution electrocatalysts

Fangyi Cheng^{1,2}, Jian Shen¹, Bo Peng¹, Yuede Pan¹, Zhanliang Tao^{1,2} and Jun Chen^{1,2*}

Spinels can serve as alternative low-cost bifunctional electrocatalysts for oxygen reduction/evolution reactions (ORR/OER), which are the key barriers in various electrochemical devices such as metal-air batteries, fuel cells and electrolyzers. However, conventional ceramic synthesis of crystalline spinels requires an elevated temperature, complicated procedures and prolonged heating time, and the resulting product exhibits limited electrocatalytic performance. In this Article, we report the synthesis of nanocrystalline $M_xMn_{3-x}O_4$ (M = divalent metals) spinels under ambient conditions and their electrocatalytic application. We show rapid and selective formation of tetragonal or cubic $M_xMn_{3-x}O_4$ from the reduction of amorphous MnO_2 in aqueous M^{2+} solution. The prepared $Co_xMn_{3-x}O_4$ nanoparticles manifest considerable catalytic activity towards the ORR/OER as a result of their high surface areas and abundant defects. The newly discovered phase-dependent electrocatalytic ORR/OER characteristics of Co-Mn-O spinels are also interpreted by experiment and first-principle theoretical studies.

As a result of their diverse properties, spinel compounds of AB_2X_4 (A,B = metal, X = chalcogen) have attracted a great deal of research interest linked to a wide range of applications including magnetism, electronics and catalysis, as well as energy storage and conversion^{1–3}. The spinel structure is known to be built around a closely packed array of X^{2-} ions, with A^{2+} and B^{3+} cations occupying part or all of the tetrahedral and octahedral sites, respectively⁴. Among the numerous varieties of spinels, MMn_2O_4 is one of the most intriguing composite oxides, because manganese has many advantages, including low cost, high abundance, low toxicity, multiple valence and prominent Jahn-Teller effect⁵. Manganese-based spinels have a range of versatile applications, including lithium insertion electrodes⁶, magnetic materials⁷ and catalysts⁸. Their physicochemical properties are highly sensitive to the composition, structural parameters, and distribution and oxidation state of cations^{5–8}, which depend greatly on the synthesis conditions. The traditional synthesis of spinel compounds generally follows a solid-state route that involves grinding and firing of a mixture of oxides, nitrates or carbonates⁹. Solid-state reactions generally require elevated temperatures or prolonged process times to overcome the diffusional barriers^{10,11}. Recently, to replace such conventional ‘brute force’ ceramic preparations, developments have been made in new approaches such as sol-gel processing¹², organic co-precipitation¹³ and flux or solvothermal strategies¹⁴. These can proceed at moderate temperatures and form metastable phases with controllable product particle size due to enhanced reaction kinetics. However, despite continuous efforts, the rapid and rational synthesis of crystalline spinels at room temperature and ambient atmosphere remains a challenge.

The oxygen reduction/evolution reactions (ORR/OER) play key roles in many energy conversion and storage technologies, including metal-air batteries, fuel cells and electrolyzers¹⁵. ORRs are sluggish in nature and traditionally require the exclusive use of

platinum-based catalysts^{15,16}. As platinum is expensive and scarce, substantial efforts have been dedicated to further improving its performance, and also to searching for non-noble metal catalysts^{17–20}. Spinels can be used as alternative and low-cost electrocatalysts for ORRs and OERs^{21,22}. However, spinels prepared by the traditional ceramic route have limited electrocatalytic activity due to their large particle size and low specific surface areas. The development of nanostructured spinels suitable for the highly efficient catalysis of ORRs/OERs is therefore of paramount importance.

In this Article, we present a facile and rapid methodology to prepare the nanocrystalline spinel $M_xMn_{3-x}O_4$ (M represents divalent metals such as Co, Mg and Zn) under ambient conditions, as well as the application of the synthesized nanoparticulate $Co_xMn_{3-x}O_4$ as a bifunctional electrocatalyst for both ORR and OER. The formation of $M_xMn_{3-x}O_4$ was accomplished by reduction of amorphous MnO_2 precursors in an aqueous solution containing M^{2+} . Amorphous MnO_2 nanoparticles were selected as precursors because they result in short diffusion distances and high surface areas for facile solid-state diffusion and interfacial contact, and also offer linked building blocks ($[MnO_6]$ octahedrons), which are partially retained as a moiety in the final product. The randomly arranged structural units in amorphous MnO_2 also aid lattice reconstruction during its transformation into crystalline spinels, because of its lower activation energy barrier. We also combine evidence from both experiment and density functional theory (DFT) to determine the high catalytic activity of the Co-Mn-O nanocrystalline spinels and the related phase-dependent electrochemical characteristics that have not been investigated previously. It was found that the cubic Co-Mn-O spinel outperforms the tetragonal phase in intrinsic ORR catalytic activity, but the tetragonal spinel surpasses the cubic phase for OER, due to the dissimilar binding energies of oxygen adsorption on cobalt and manganese defect sites.

¹Institute of New Energy Material Chemistry, Chemistry College, Nankai University, Tianjin 300071, China, ²Key Laboratory of Advanced Energy Materials Chemistry (Ministry of Education), Chemistry College, Nankai University, Tianjin 300071, China. *e-mail: chenabc@nankai.edu.cn

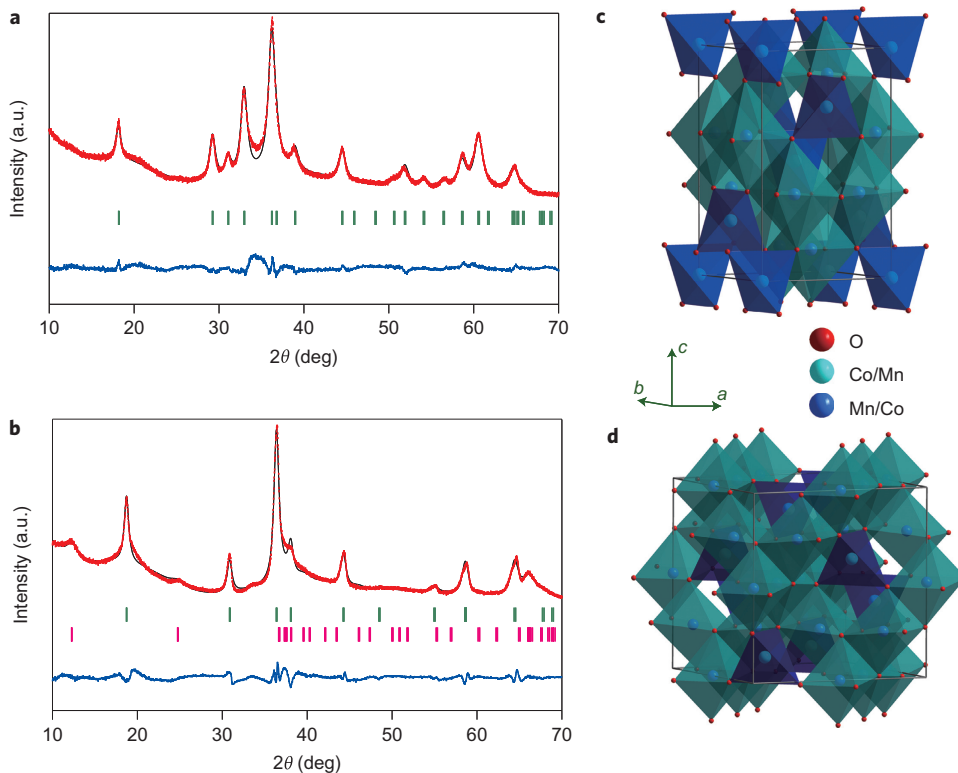


Figure 1 | Structural analysis of the synthesized nanocrystalline spinels. **a,b**, Rietveld refined XRD patterns of **CoMnO-B** (**a**) and **CoMnO-P** (**b**) with experimental data (red dots), calculated profiles (black line), allowed Bragg diffraction positions (vertical bars) and difference curve (blue line). **c,d**, Schematic representation of tetragonal (**c**) and cubic (**d**) spinels.

Results and discussion

We have achieved the room-temperature synthesis of manganese-based spinels by chemical reduction of MnO_2 in the presence of metal ions. The amorphous MnO_2 precursor with a mean manganese valence of 3.7 was first prepared in a one-step redox reaction between KMnO_4 and $\text{Mn}(\text{CH}_3\text{COO})_2$ in alkaline aqueous solution (Supplementary Figs S1 and S2). Two representative nanocrystalline $\text{Co}_x\text{Mn}_{3-x}\text{O}_4$ spinels, **CoMnO-P** and **CoMnO-B**, were then synthesized using NaH_2PO_2 and NaBH_4 as reductants, respectively.

Figure 1 shows the X-ray diffraction (XRD) patterns and corresponding Rietveld analysis of as-prepared samples, confirming the formation of spinel phases. The broadened peaks were attributed to the nanoscale grain present in the product. For **CoMnO-B** (Fig. 1a), all the reflections were indexable on the basis of space group $I41/amd$ (no. 141) and coincided with the standard values of tetragonal CoMn_2O_4 (Joint Committee on Powder Diffraction Standards, JCPDS card no. 77-471). The low reliability factor indicated that the Rietveld refined XRD pattern fitted quite well with the experimental data points, giving calculated cell parameters of $a = b = 5.759(2)$ Å and $c = 9.252(4)$ Å. Combining the refined results and elemental analysis, the structural formula of **CoMnO-B** was determined to be tetragonal $(\text{Co})_{4a}[\text{Co}_{0.1}\text{Mn}_{1.9}]_{8d}\text{O}_4$ (Supplementary Table S1). For **CoMnO-P** (Fig. 1b), refinement revealed the coexistence of a major cubic spinel phase (63 wt%) and a minor monoclinic birnessite phase (37 wt%), with formulas expressed as $(\text{Co}_{0.36}\text{Mn}_{0.35}\text{Y}_{0.29})_{8a}[\text{Co}_{0.92}\text{Mn}_{1.00}\text{Y}_{0.08}]_{16d}\text{O}_4$ (Y denotes vacancy) and $\text{Na}_{0.22}\text{MnO}_2(\text{H}_2\text{O})_{1.32}$, respectively (Supplementary Tables S2 and S3). In comparison with traditional, high-temperature spinels, **CoMnO-B** had larger cell parameters, whereas **CoMnO-P** had a shrunken lattice due to the presence of ionic vacancies (Supplementary Fig. S3 and Table S4).

Figure 2a,b shows typical scanning electron microscopy (SEM) images of the spinel product. The nanoparticulate morphology of

the amorphous MnO_2 precursor (Supplementary Fig. S4) is basically preserved. The average particle size of **CoMnO-P** increased from ~ 70 nm to 110 nm, whereas **CoMnO-B** demonstrated a reticular and porous texture. The interconnected porous structure of **CoMnO-B** could be attributed to hydrogen bubbling from the reaction between MnO_2 and BH_4^- . The clear fringes observed in transmission electron microscopy (TEM) images and the corresponding fast Fourier transform (FFT) diffraction pattern (Fig. 2c,d) indicate the crystallinity of the synthesized nanoparticles, in spite of the presence of numerous defects. The measured neighbouring interlayer distance in **CoMnO-P** was consistent with the spacing between the (011) planes of the single tetragonal CoMn_2O_4 spinel phase, confirming the XRD analysis. TEM imaging of **CoMnO-P** also determined the coexisting phases of cubic spinel and monoclinic birnessite, with indexed planes of (111) and (202), respectively. The well-defined points in the FFT pattern agree with the allowed Bragg diffraction of cubic spinel. Furthermore, results from the energy-dispersive spectra (EDS) of **CoMnO-P** (Fig. 2e) and **CoMnO-B** (Fig. 2f) confirm the elemental composition determined from atomic absorption spectroscopy.

Three points are worth highlighting regarding the present synthesis of nanocrystalline spinels. First, the synthesized phase was determined by the reducing ability of the applied reductant. Strong reducing agents such as NaBH_4 and $\text{N}_2\text{H}_4\cdot\text{H}_2\text{O}$ (Supplementary Fig. S5) resulted in tetragonal spinels with the composition of CoMn_2O_4 . In contrast, when NaH_2PO_2 , with its relatively weak reducing power, was used, Mn(IV) in the MnO_2 precursor was only partially reduced to form a cubic phase, and the remaining high-valence manganese resulted in a birnessite phase. This phase selectivity could be explained by taking into account the fact that Mn(III) (d^4) tends to Jahn-Teller distortion⁵, and thus induces lower crystallographic symmetry. The second point is that phase speciation of spinels was accomplished within a short

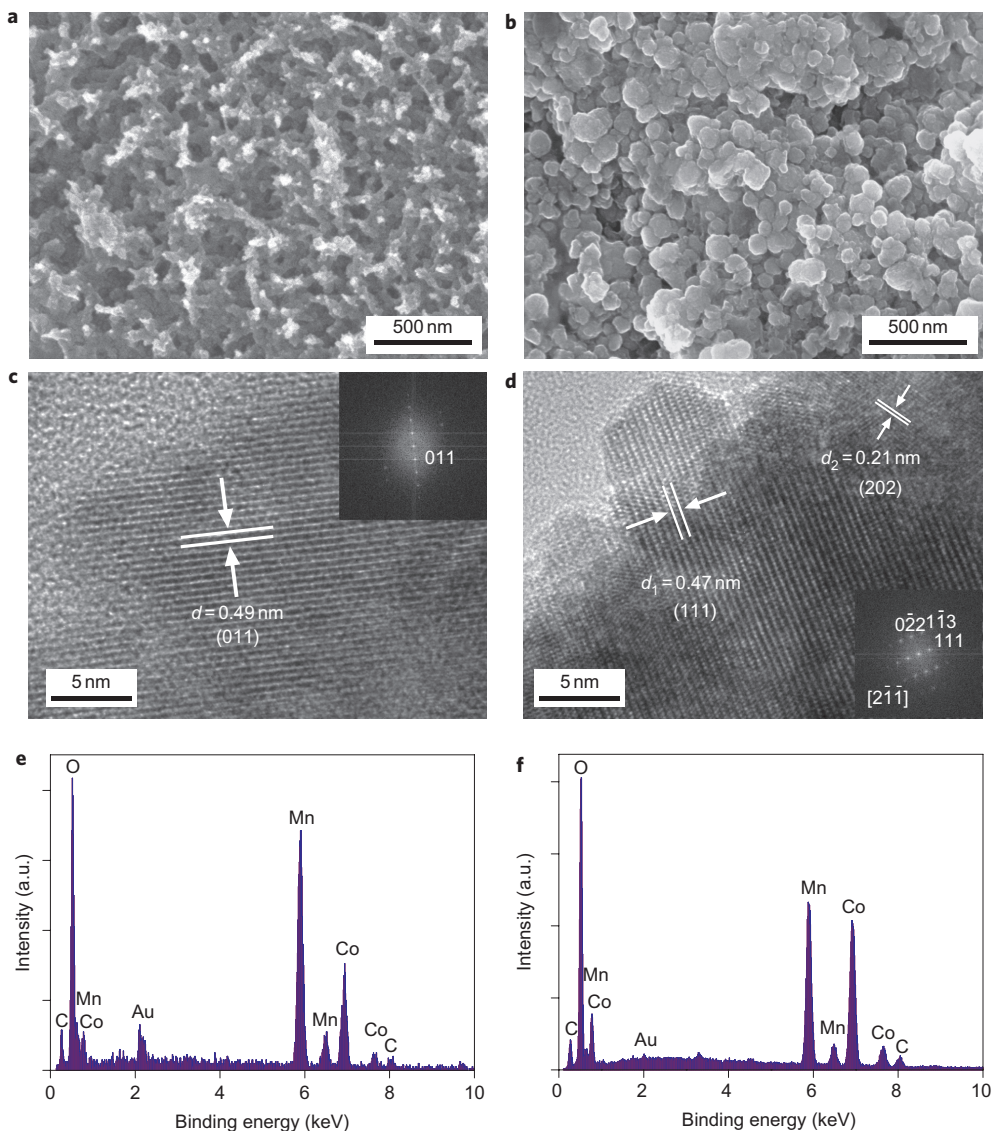


Figure 2 | Characterization of CoMnO-B and CoMnO-P. **a,b**, SEM images showing the porous nanostructures of CoMnO-B (**a**) and the nanoparticulate morphology of CoMnO-P (**b**). **c,d**, High-resolution TEM images and the corresponding FFT patterns (inset), showing the single tetragonal spinel phase (**c**) and the double phases of cubic spinel and monoclinic birnessite (**d**). **e,f**, EDS spectra confirming the elemental ratio of cobalt to manganese.

time (5 min; Supplementary Fig. S6), enabling a rapid synthesis that is barely achievable using traditional high-temperature ceramic routes⁹. Third, the non-crystallinity of the MnO₂ precursor is a critical influential factor in obtaining a spinel product under ambient conditions. High-purity spinels could be prepared only from amorphous MnO₂ rather than from crystalline MnO₂ (Supplementary Fig. S2), because in the latter case the formation of spinel requires more energy to overcome the higher energy barrier accompanying the collapse of the ordered parent crystal lattice. Increasing the concentration of reducing agent or elevating the reaction temperature could enhance the crystallinity of the formed spinels (Supplementary Table S5). Furthermore, it is possible to adjust spinel morphology by altering the shape of the precursor. In addition to nanoparticles, interconnected wirelike Co–Mn–O nanostructures were also fabricated using electro-deposited amorphous MnO₂ nanowires (Supplementary Fig. S7).

The question emerging from this experiment is why nanocrystalline spinels can be formed at room temperature and under ambient pressure. We found that, in the absence of Co²⁺, the reduction of amorphous MnO₂ resulted in high-purity Mn₃O₄ with a typical

tetragonal spinel phase (Supplementary Fig. S8). The standard Gibbs free energy change of the pertinent reaction ($3 \text{MnO}_2 + \text{BH}_4^- \rightarrow \text{Mn}_3\text{O}_4 + \text{BO}_2^- + 2 \text{H}_2$) is -681 kJ mol^{-1} , indicating that the formation of spinel from MnO₂ is thermodynamically feasible (see Supplementary Information). Accordingly, we propose a reduction-crystallization mechanism for the synthesis of $\text{Co}_x\text{Mn}_{3-x}\text{O}_4$. The Mn(IV) in the amorphous nanoparticulate MnO₂ precursor is rapidly reduced to lower-valence manganese (Mn(III) and/or Mn(II)) by a strong reducing agent²³, and the amorphous MnO₂ structure is transformed to the spinel phase. At the same time, the dissociative Co²⁺ in the solution diffuses into the solid lattice and either occupies the manganese vacancies or partially substitutes for manganese ions in the tetrahedral or octahedral inter-space²⁴. The driving force of such ion exchange is the ‘site preference energies’ of transition-metal ions in the spinel crystal lattices, according to crystal field theory^{25,26}. The Co–Mn–O solid solution spontaneously crystallizes into the final nanocrystalline spinel and maintains the essential morphology of the precursor. Based on this postulated synthetic route, we have also successfully prepared ZnMn₂O₄ and MgMn₂O₄ crystalline nanoparticles

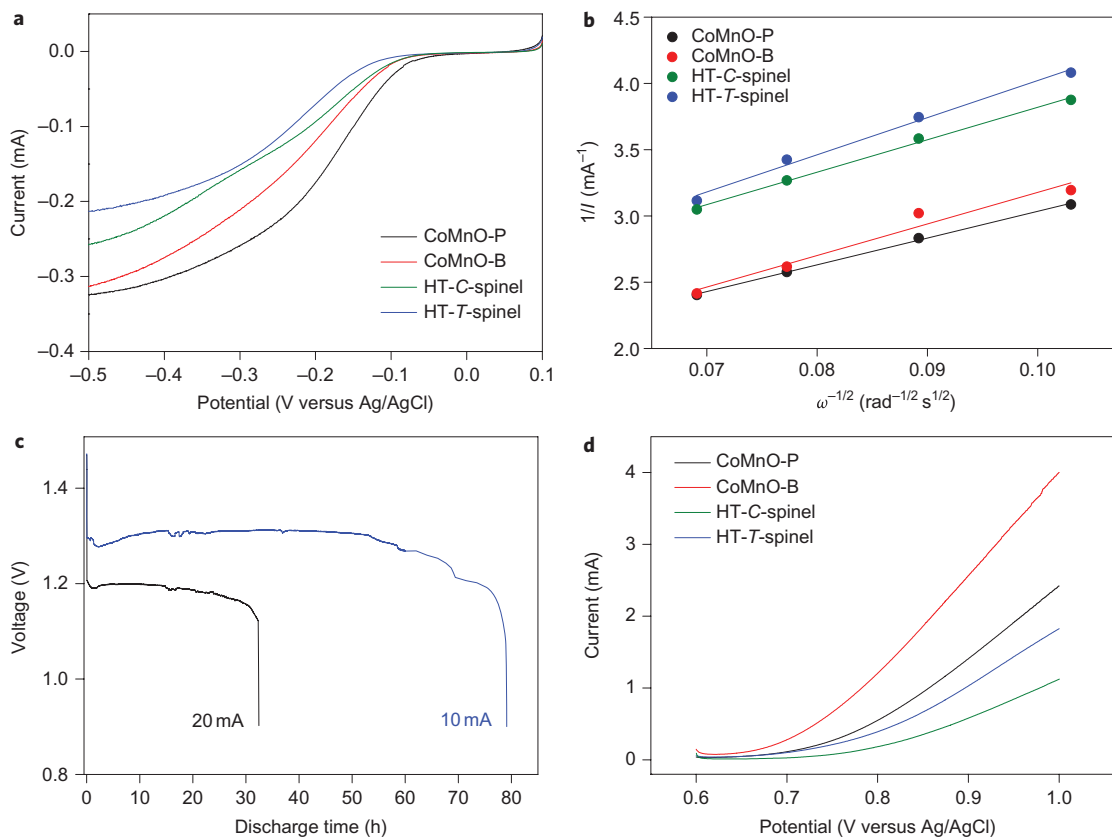


Figure 3 | Electrochemical application of nanocrystalline CoMnO-B and CoMnO-P as ORR and OER electrocatalysts. **a**, Voltammograms of the ORR using catalyst-modified RDEs in O_2 -saturated alkaline electrolyte. **b**, K-L plots for the ORR. **c**, Galvanostatic discharge curves of the prototype zinc-air battery made with a nanoparticle catalyst layer. **d**, Voltammetry curves of the OER measured at different catalyst-modified electrodes.

through similar procedures by simply replacing Co^{2+} with Zn^{2+} and Mg^{2+} , respectively (Supplementary Fig. S9).

Because of the nanoparticulate texture, the prepared representative **CoMnO-B** and **CoMnO-P** spinels had Brunauer–Emmett–Teller (BET) surface areas of 112 and 122 $m^2 g^{-1}$, respectively, which are significantly higher than those of the tetragonal $CoMn_2O_4$ (denoted **HT-T-spinel**) and cubic Co_2MnO_4 (denoted **HT-C-spinel**) powders synthesized using the traditional high-temperature method (Supplementary Figs S10 and S11). The featured high specific surface areas and numerous defects of nanocrystalline spinels motivated us to further investigate their catalytic performance for ORR/OER.

Figure 3 shows the ORR and OER catalytic characteristics recorded on glass carbon electrodes loaded with the **CoMnO-B** and **CoMnO-P** nanoparticles and the corresponding high-purity spinel powders synthesized at high temperature. As shown in Fig. 3a, the representative linear sweeping voltammograms of the ORR, measured on rotating disk electrodes (RDEs), exhibited similar profiles, with two regions of potential–current response. Scanning the potential cathodically, the detected currents increased rapidly in the mixed kinetic–diffusion control region (approximately -0.1 to -0.3 V) and then slowed down, with the appearance of diffusion-limiting currents (I_d). As has been reported for other transition-metal oxides^{27,28}, the observed current was attributed to catalytic oxygen reduction through comparison with polarization curves recorded on the electrodes without catalyst modification or in the absence of oxygen, which showed no distinguishable cathodic current over the tested potential range (Supplementary Figs S12 and S13). Evidently, the room-temperature nanocrystalline spinels outperformed the corresponding high-temperature spinel powders in terms of more positive onset potential and larger current value. Furthermore, the cubic

phase exhibited lower overpotential than did the tetragonal phase (Supplementary Figs S14 and S15).

To quantitatively analyse the catalytic ORR, four sets of voltammetry curves were recorded on RDEs at different speeds of rotation (Supplementary Fig. S13). The current increased with rising rotational rates ω as a result of the faster oxygen flux to the electrode surface. The observed rotation-speed-dependent current I can be theoretically expressed by the Koutecky–Levich (K–L) equation²⁹ for analysing ORR kinetics (see Supplementary Information). Figure 3b shows the constructed K–L curves, which plot $1/I$ versus $\omega^{-1/2}$ at -0.5 V, where the transferred electron number per oxygen molecule (n) in the ORR can be calculated from the slopes of the fitted linear line. Lower n values indicate inferior performance. These results suggest an apparent quasi-four-electron process on nanocrystalline spinels, which is desirable for achieving high-efficiency electrocatalytic ORR. Among the spinels, catalytic activity decreased in the order **CoMnO-P** > **CoMnO-B** > **HT-C-spinel** > **HT-T-spinel**. As the two high-temperature samples were of high purity, comparison of their performance directly reflects the different intrinsic activities of the cubic and tetragonal phases. For spinels with the same phase, room-temperature nanoparticles outperform their high-temperature counterparts. Such superior activity could be largely attributed to the higher specific surface areas of nanocrystalline spinels providing more active sites for heterogeneous ORR catalysis.

For the nanocrystalline spinels, the steady currents observed in the continuous polarization period of 2 h (Supplementary Fig. S16) provided preliminary evidence of catalytic stability in an alkaline medium, which is consistent with previous results for manganese-based oxides³⁰. The ORR performance of the four spinel samples was compared with the benchmark carbon-supported platinum nanoparticles (Pt/C) (Supplementary Fig. S17 and Table S6). Surprisingly,

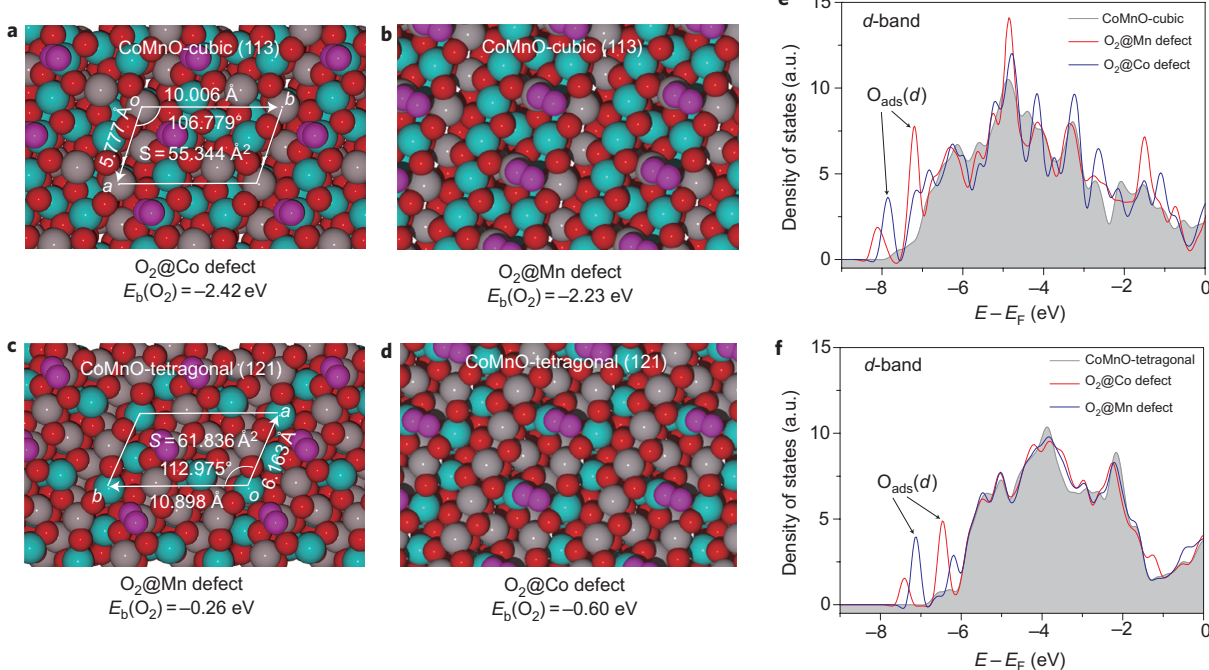


Figure 4 | First-principle study of surface oxygen adsorption on different sites of cubic and tetragonal spinel phases. **a–d**, Geometries and binding energies of oxygen molecules (purple) on cobalt (cyan) or manganese (grey) defect sites. Red spheres represent lattice oxygen. **e,f**, Corresponding density of states of bare and O_2 -adsorbed spinels.

the nanoparticulate spinels exhibited currents and apparent transferred electron numbers close to those of the Pt/C catalyst. The relatively lower onset potential for the spinels could be improved by cation doping or metal decorating to modify the surface electronic properties or enhance conductivity^{31,32}. The nanocrystalline spinels also demonstrated favourable ORR activity in neutral KCl electrolytes (Supplementary Fig. S18). Furthermore, the most active **CoMnO-P** was used in an air electrode to construct a laboratory coin-type zinc-air cell, which delivered a stable galvanostatic discharge curve and considerable specific energy densities (Fig. 3c; Supplementary Fig. S19). Therefore, it is clear that nanocrystalline spinels synthesized at room temperature should find a practical application in metal-air batteries.

Spinel metal oxides have been widely investigated as a catalyst for OER¹⁵, so we next measured the quasi-steady polarization curves in a solution of 0.1 M KOH in the potential range 0.6–1.0 V (Fig. 3d). Again, the room-temperature spinel nanoparticles exhibited higher activity than the corresponding high-temperature powders. Of particular interest is that, for both nanoparticles and powders, the tetragonal spinel phase generates an OER current nearly twice that of the cubic phase, which is in contrast with the results for ORR. To the best of our knowledge, phase-dependent ORR and OER electrocatalytic properties have not been reported previously for spinels.

In general, it has been proposed that electrocatalytic ORR in alkaline media proceeds through multistep reactions involving, first, the formation of an HO_2^- intermediate from adsorbed O_2 on the active sites of the catalyst surface, followed by its further reduction or decomposition to OH^- ions^{27,28}. Catalysis of the ORR correlates with the number of available catalytic sites and the absorption affinity for oxygen^{15,18,19,33}. To elucidate the differences in the intrinsic activities of the cubic and tetragonal spinels, we performed X-ray photoelectron spectroscopy (XPS) and temperature programmed desorption (TPD) analysis (Supplementary Figs S20 and S21). The results suggest that the cubic phase has a stronger oxygen binding ability than the tetragonal phase.

To gain further insight into the relationships between ORR activity and the phase or defects of the Co–Mn–O spinel system,

we conducted a series of DFT calculations (see computational details in the Supplementary Information) to study the oxygen adsorption on different defect sites of two typical surfaces, cubic (113) and tetragonal (121). Figure 4a–d displays the binding energies (E_b) of an oxygen molecule on Co/Mn defect sites of the as-investigated spinel phases. It is clear that the cobalt defect site can bind oxygen a little more strongly than the manganese defect site, whereas, on either the cobalt or manganese sites, the cubic (113) surface generates much more stable molecular oxygen adducts than the tetragonal (121) surface. Figure 4e,f presents oxygen adsorption characteristics from the electron structure analysis aspect. In comparison with the tetragonal spinel, the cubic phase shows an increase in the adsorbed oxygen (O_{ads})-induced d -band, indicating a strengthened metal– O_2 bond. Furthermore, the investigated surfaces of both phases contain the same number of catalytic sites per surface unit cell, but the area of the cubic (113) unit cell is smaller. Therefore, for a given surface area, the number of available active sites on the cubic (113) surface will exceed that on the tetragonal (121) surface. Accordingly, this can be interpreted to indicate that the cubic Co–Mn–O spinel outperforms the tetragonal phase in intrinsic ORR catalytic activity. Similarly, regarding electrocatalytic OER, one can predict that the performance of the tetragonal spinel surpasses the cubic phase, because the OER can be viewed as a reverse process of the ORR¹⁵.

Conclusions

Rapid synthesis of nanocrystalline $M_x\text{Mn}_{3-x}\text{O}_4$ ($M = \text{Co}, \text{Mg}, \text{Zn}$, and so on) spinels at room temperature was realized using a reduction–recrystallization route with amorphous MnO_2 nanoparticle precursors. The obtained $\text{Co}_x\text{Mn}_{3-x}\text{O}_4$ spinel, with controllable crystallographic phase of either the cubic or tetragonal form, inherits the essential morphology of the parent MnO_2 , demonstrating high specific surface areas and abundant defects. When applied as an electrocatalyst for both ORR and OER, the room-temperature nanoparticles outperform the corresponding high-temperature powders. The intrinsic electrocatalytic activity of cubic and

tetragonal Co–Mn–O spinels correlates with the oxygen binding ability on the catalyst surface, as indicated from both experimental analysis and DFT theoretical calculations. These results should aid in the rational design and facile preparation of a spinel-based ORR/OER bifunctional electrocatalyst to be used in the air electrodes that are widely used in metal–air batteries and fuel cells.

Methods

Synthesis. To obtain amorphous MnO₂ nanoparticle precursors, Mn(CH₃COO)₂ (100 ml, 0.03 M) was added to KMnO₄ solution (50 ml, 0.04 M, adjusted pH value of 12) at room temperature. The formed brown deposit was filtered, washed with water, and dried overnight at 60 °C. In a typical synthesis of nanocrystalline Co_xMn_{3-x}O₄ spinel, amorphous MnO₂ (0.348 g) and CoCl₂·6H₂O (0.476 g) were mixed in 20 ml of water. Under vigorous magnetic stirring, an excess amount of freshly prepared NaBH₄ solution (NaBH₄ dissolved in NaOH solution, pH = 11–12) was then added dropwise to the mixture at controlled temperature. The violet-red solution immediately turned colourless, with severe bubbling. The resulting precipitate was collected by centrifugation, washed repeatedly with distilled water to remove residual ions, and vacuum-dried at 80 °C for 12 h. Similar procedures were adopted when using NaH₂PO₂ or N₂H₄·H₂O as the reductant. For the synthesis of MgMn₂O₄ and ZnMn₂O₄, MgCl₂ and ZnCl₂ aqueous solutions were used as the starting magnesium and zinc sources, respectively.

Characterization. XRD patterns were recorded on a Rigaku D/max-2500 X-ray diffractometer (Cu K α radiation, λ = 1.5406 Å), in a 2θ angular range of 10–80° with a velocity of 0.02° in 4 s. The XRD profiles were refined using the Rietveld refinement program RIETAN-2000 (ref. 34). Chemical composition was determined by atomic absorption spectrometry (AAS, Hitachi 180-80 spectrophotometer) and EDS. SEM images were obtained using a JEOL JSM-6700F microscope (operating voltage, 10 kV) equipped with an EDS spectrometer. TEM and HRTEM images were collected on a Tecnai F20 (200 keV) microscope. Textural characterization was carried out by measuring the N₂ adsorption/desorption isotherms at 77 K on a Bell-mini instrument. XPS data were collected using a Perkin Elmer PHI 1600 ESCA system. TPD/MS analysis was performed on an Autosorb-IC-TCD-MS system with a Prismplus QME 220 MS detector (Quantachrome) under helium gas flow.

Electrochemical test. Electrochemical measurements were conducted using a three-electrode cell. A glassy carbon disk electrode with coated catalysts was used as the working electrode. The catalyst was composed of well-mixed 30 wt% Co_xMn_{3-x}O₄ samples and 70 wt% carbon powders (Vulcan XC 72). The preparation of catalyst-modified electrodes and determination of the weight of active materials followed procedures similar to those reported in our previous work³⁵. An Ag/AgCl electrode (with a nominal potential of 0.197 V versus reversible hydrogen electrode) in saturated KCl aqueous solution and a platinum wire were used as the reference and counterelectrodes, respectively. The electrolyte comprised a 0.1 M aqueous KOH or KCl solution. Electrochemical tests were carried out at room temperature on a Parstat 2273 potentiostat/galvanostat workstation assembled with a model 636 rotational system (AMETEK). The linear sweep voltammetry was obtained at a scan rate of 1 mV s⁻¹ in the potential range 0.1 to -0.5 V (ORR) or 0.6–1.0 V (OER). In the ORR experiment, the electrolyte was bubbled with high-purity O₂ for 30 min before each test and maintained under atmospheric conditions with constant O₂ gas flow during the measurements. The zinc–air cell was assembled with a zinc anode, a cellulose separator and an air cathode consisting of a spinel catalyst layer. Measurements were carried out on the as-fabricated cell at room temperature (near 25 °C) with a land battery testing system.

Received 15 June 2010; accepted 10 November 2010;
published online 12 December 2010

References

1. Hemberger, J. *et al.* Relaxtor ferroelectricity and colossal magnetocapacitive coupling in ferromagnetic CdCr₂S₄. *Nature* **434**, 364–367 (2005).
2. Fan, H. J. *et al.* Monocrystalline spinel nanotube fabrication based on the Kirkendall effect. *Nature Mater.* **5**, 627–631 (2006).
3. Matsuda, M. *et al.* Spin-lattice instability to a fractional magnetization state in the spinel HgCr₂O₄. *Nature Phys.* **3**, 397–400 (2008).
4. Bragg, W. H. The structure of magnetite and spinels. *Nature* **95**, 561 (1915).
5. Shoemaker, D. P., Li, J. & Seshadri, R. Unraveling atomic position in an oxide spinel with two Jahn–Teller ions: local structure investigation of CuMn₂O₄. *J. Am. Chem. Soc.* **131**, 11450–11457 (2009).
6. Thackeray, M. M. Manganese oxides for lithium batteries. *Prog. Solid State Chem.* **25**, 1–71 (1997).
7. Choi, H. C., Shim, J. H. & Min, B. I. Electronic structures and magnetic properties of spinel ZnMn₂O₄ under high pressure. *Phys. Rev. B* **74**, 172103 (2006).
8. Fierro, G. *et al.* H₂ reduction behavior and NO/N₂O abatement catalytic activity of manganese based spinels doped with copper, cobalt and iron ions. *Catal. Today* **116**, 38–49 (2006).

9. Armijo, J. S. The kinetics and mechanism of solid-state spinel formation—a review and critique. *Oxid. Met.* **1**, 171–198 (1969).
10. Stein, A., Keller, S. W. & Mallouk, T. E. Turning down the heat: design and mechanism in solid-state synthesis. *Science* **259**, 1558–1564 (1993).
11. Wiley, J. B. & Kaner, R. B. Rapid solid-state precursor synthesis of materials. *Science* **255**, 1093–1097 (1992).
12. Lavela, P., Tirado, J. L. & Vidal-Abarca, C. Sol-gel preparation of cobalt manganese mixed oxides for their use as electrode materials in lithium cells. *Electrochim. Acta* **52**, 7986–7995 (2007).
13. Rojas, R. M. *et al.* Thermal behaviour and reactivity of manganese cobaltites Mn_xCo_{3-x}O₄ (0.0 < x < 1.0) obtained at low temperature. *J. Mater. Chem.* **4**, 1635–1639 (1994).
14. Matsushita, Y., Ueda, H. & Ueda, Y. Flux crystal growth and thermal stabilities of LiV₂O₄. *Nature Mater.* **4**, 845–850 (2005).
15. Kinoshita, K. *Electrochemical Oxygen Technology* (Wiley, 1992).
16. Steele, B. C. H. & Heinzl, A. Materials for fuel-cell technologies. *Nature* **414**, 345–352 (2001).
17. Lim, B. *et al.* Pd–Pt bimetallic nanodendrites with high activity for oxygen reduction. *Science* **324**, 1302–1305 (2009).
18. Greeley J. *et al.* Alloys of platinum and early transition metals as oxygen reduction electrocatalysts. *Nature Chem.* **1**, 552–556 (2009).
19. Strasser, P. *et al.* Lattice-strain control of the activity in dealloyed core–shell fuel cell catalysts. *Nature Chem.* **2**, 454–460 (2010).
20. Bashyam, R. & Zelenay, P. A class of non-precious metal composite catalysts for fuel cells. *Nature* **443**, 63–66 (2006).
21. Rios, E., Gautier, J. L., Poillerat, G. & Chartier, P. Mixed valency spinel oxides of transition metals and electrocatalysis: case of the Mn_xCo_{3-x}O₄ system. *Electrochim. Acta* **44**, 1491–1497 (1998).
22. Cong, H. N., Abbassi, K. & Chartier, P. Electrocatalysis of oxygen reduction on polypyrrole/mixed valence spinel oxide nanoparticles. *J. Electrochem. Soc.* **149**, A525–A530 (2002).
23. Ganem, B. & Osby, J. O. Synthetically useful reactions with metal boride and aluminide catalysts. *Chem. Rev.* **86**, 763–780 (1986).
24. Burns, R. G. The uptake of cobalt into ferromanganese nodules, soils, and synthetic manganese (iv) oxides. *Geochim. Cosmochim. Acta* **40**, 95–102 (1976).
25. Shubin, M. S., Litinskii, A. O., Popov, G. P. & Men, A. N. Cation-distribution preference energy in crystals formed by binary oxides of transition metals with the spinel structure. *J. Struct. Chem.* **17**, 133–138 (1976).
26. Burdett, J. K., Price, G. D. & Price, S. L. Role of the crystal-field theory in determining the structures of spinels. *J. Am. Chem. Soc.* **104**, 92–95 (1982).
27. El-Deab, M. S. & Ohsaka, T. Manganese oxide nanoparticles electrodeposited on platinum are superior to platinum for oxygen reduction. *Angew. Chem. Int. Ed.* **45**, 5963–5966 (2006).
28. Chainet, I. R., Chatenet, M. & Vondrák, J. Carbon-supported manganese oxide nanoparticles as electrocatalysts for the oxygen reduction reaction (ORR) in alkaline medium: physics characterizations and ORR mechanism. *J. Phys. Chem. C* **111**, 1434–1443 (2007).
29. Yamamoto, K. *et al.* Size-specific catalytic activity of platinum clusters enhances oxygen reduction reactions. *Nature Chem.* **1**, 397–402 (2009).
30. Roche, I., Chainet, E., Chatenet, M. & Vondrák, J. Durability of carbon-supported manganese oxide nanoparticles for the oxygen reduction reaction (ORR) in alkaline medium. *J. Appl. Electrochem.* **38**, 1195–1201 (2008).
31. Stamenkovic, V. *et al.* Trends in electrocatalysis on extended and nanoscale Pt-bimetallic alloy surfaces. *Nature Mater.* **6**, 241–247 (2007).
32. Cheng, F. Y. *et al.* MnO₂-based nanostructures as catalyst for electrochemical oxygen reduction in alkaline media. *Chem. Mater.* **22**, 898–905 (2010).
33. Rios, E. *et al.* Electrocatalysis of oxygen reduction on Cu_xMn_{3-x}O₄ (1 ≤ x ≤ 1.4) spinel particles/polypyrrole composite electrodes. *Int. J. Hydrogen Energy* **33**, 4945–4954 (2008).
34. Izumi, F. & Ikeda, T. A rietveld-analysis program RIETAN-98 and its application to zeolites. *Mater. Sci. Forum* **321–324**, 198–203 (2000).
35. Cheng, F. Y. *et al.* Selective synthesis of manganese oxide nanostructures for electrocatalytic oxygen reduction. *ACS Appl. Phys. Interf.* **1**, 460–466 (2009).

Acknowledgements

This work was supported by the Programs of National NSFC (20873071), MOST (2011CB935902), MOE Innovation Team (IRT0927), Tianjin High-Tech (08JCZDJC21300) and the Fundamental Research Funds for the Central Universities.

Author contributions

F.C., J.S. and Y.P. synthesized and characterized the materials. F.C. and J.S. carried out electrochemical measurements. B.P. performed the first-principles simulation. All authors contributed to the data analysis. J.C. directed the research.

Additional information

The authors declare no competing financial interests. Supplementary information accompanies this paper at www.nature.com/naturechemistry. Reprints and permission information is available online at <http://npg.nature.com/reprintsandpermissions/>. Correspondence and requests for materials should be addressed to J.C.